PNAS
www.pnas.org

Supplementary Information for

Contact mechanics between the human finger and a touchscreen under electroadhesion

Mehmet Ayyildiz, Michele Scaraggi, Omer Sirin, Cagatay Basdogan, Bo N.J. Persson

Bo N.J. Persson.
E-mail: b.persson@fz-juelich.de

This PDF file includes:

www.pnas.org/cgi/doi/10.1073/pnas.1811268115

Supporting Information Text

Here we report the computational contact model (formulation, resolution algorithm and model validation) for electroadhesion used in the main paper to validate the mean field contact mechanics. Furthermore, we report supplemental theoretical details on the voltage frequency dependence of friction, as well as on the probability density functions of interface fields.

Computational contact model for the human skin/touchscreen interaction

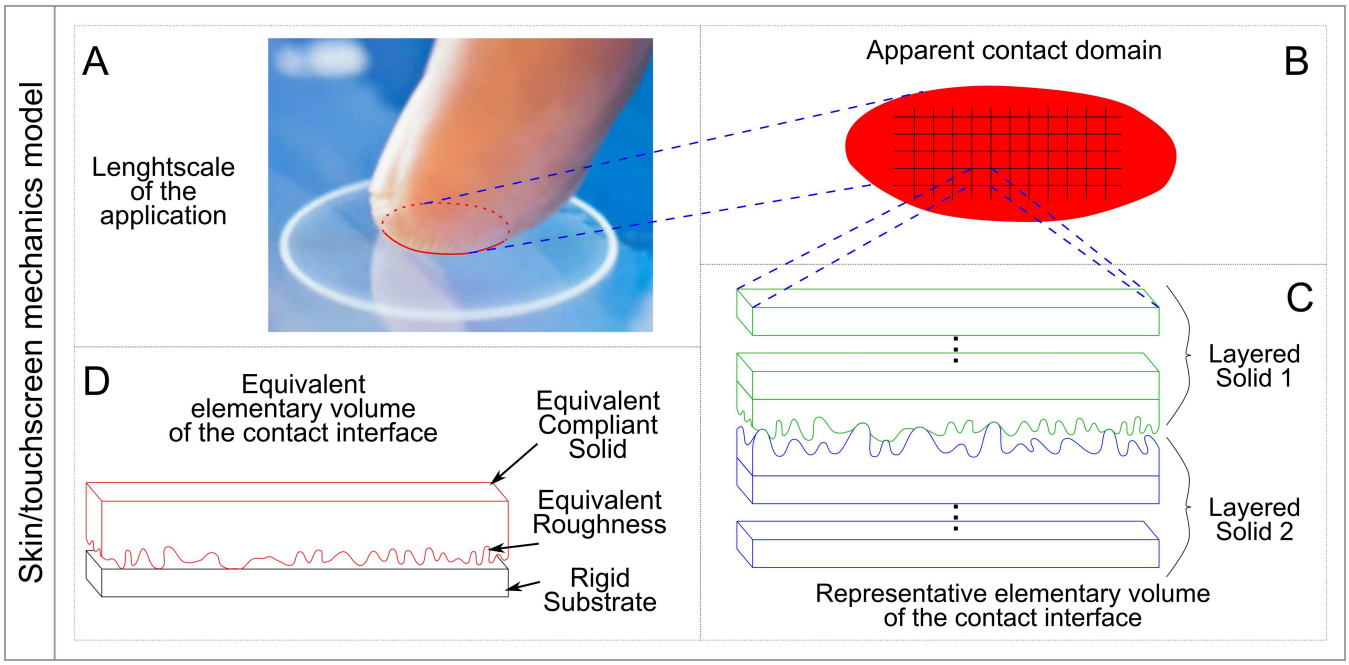

Fig. S1. Skin/touchscreen computational contact model characteristics. In the figure panel we report an overall schematic description of the multiscale skin/touchscreen contact interface: The large separation of length scales between the apparent contact domain (B) and the largest roughness wavelength (C) allows to formulate the interface mechanics by decoupling the microscale- from the macroscale- contact mechanics. The computational contact model is thus formulated to study the contact scale (C), known as the representative elementary volume of interface roughness. In the microscale model, (C), any generic rheological layering of the interface, such as the skin and touchscreen layering, can be reduced to an equivalent but simplified interface model, shown in the schematic (D).

Summary of the computational model. In Fig. S1(A)-(C) we schematically show the three length scales characterizing the finger/counter-surface interaction (A). B) shows the macroscopic contact area, which appears smooth when observed at the length scale of the application. In the finger/counter-surface contact, the macroscopic contact size, say L, is much larger than the larger roughness wavelength, say L_0. This large separation of length scales allows us to study separately the micro-contact dynamics occurring at the scale of the representative elementary interface volume (with lateral size $L_{\mathrm{REV}} \gg L_0$) from the macro-scale contact dynamics. The investigation of the micro-contact dynamics allows to determine the effective micro-scale contact mechanics properties (such as normalized contact area and average interface separation as a function of the locally-averaged contact pressure) to be used in a homogenized formulation of the macroscale contact equations. Indeed, in the latter formulation, the roughness is taken into account thanks to the effective micro-scale contact mechanics properties, resulting in a contact formulation which is smoother, and which requires a reduced computational effort than the full-scale contact formulation. In the following, we will provide the computational micro-contact model for the skin-touchscreen interaction.

We assume the roughness in normal frictionless contact with $L_{\mathrm{REV}} \approx L_0$, and the roughness to be periodic (with period L_0 in both x- and y-directions). For this case, we stress that the effective micro-scale contact mechanics properties can be obtained by averaging over multiple roughness realizations. Furthermore, we consider the case where the interacting solids show a graded rheology in a direction normal to the local average contact plane, see Fig. S1(C). The bulk rheology is assumed linear, whereas surface plasticity is taken into account with a simple plastic deformation model (see below). Small slope roughness also applies, so that $\left\langle \nabla h(\mathbf{x})^2 \right\rangle \ll 1$, where $h(\mathbf{x})$ is the surface roughness, and with $\langle h \rangle = 0$.

Within these assumptions, one can easily show that the case of Fig. S1(C) is equivalent to the case of Fig. S1(D) (1–3). The latter is characterized by the interaction between a rigid ideally smooth substrate and an equivalent compliant solid covered by an equivalent roughness. The local interface separation $u(\mathbf{x})$, corresponding to the local distance between the mating surfaces, can be agreed to be

$$u(\mathbf{x}) = \bar{u} + w(\mathbf{x}) - (h(\mathbf{x}) - w_{\mathrm{pl}}(\mathbf{x}) + \bar{w}_{\mathrm{pl}}), \qquad [A1]$$

where $\bar{u}$ is the average interface separation, $w(\mathbf{x})$ the surface elastic normal displacement, $h(\mathbf{x})$ the surface roughness, with $\langle w(\mathbf{x}) \rangle = \langle h(\mathbf{x}) \rangle = 0$. The surface plasticity is taken into account with the plastic displacement $w_{\mathrm{pl}}(\mathbf{x})$, with $\bar{w}_{\mathrm{pl}} = \langle w_{\mathrm{pl}}(\mathbf{x}) \rangle$.

We define the following Fourier transform ($\mathbf{q}$ is the transformed variable of $\mathbf{x}$)

$$w(\mathbf{q}) = (2\pi)^{-2} \int d^2\mathbf{x}\; w(\mathbf{x})\, e^{-i\mathbf{q}\cdot\mathbf{x}}$$

and

$$\sigma(\mathbf{q}) = (2\pi)^{-2} \int d^2\mathbf{x}\; \sigma(\mathbf{x})\, e^{-i\mathbf{q}\cdot\mathbf{x}},$$

where $\sigma(\mathbf{x})$ is the interface pressure distribution ($\sigma_0 = \langle\sigma(\mathbf{x})\rangle$ is the average pressure), given by the sum of the contact pressure field $\sigma_c(\mathbf{x})$ and the electroadhesive stress $\sigma_{adh}(\mathbf{x})$

$$\sigma(\mathbf{x}) = \sigma_c(\mathbf{x}) + \sigma_{adh}(\mathbf{x}). \qquad [A2]$$

Following the discussion reported in Ref. (4), $w(\mathbf{x})$ can be related to $\sigma(\mathbf{x})$ through a simple equation in the Fourier space

$$w(\mathbf{q}) = M_{zz}(\mathbf{q})\,\sigma(\mathbf{q}), \qquad [A3]$$

where $M_{zz}(\mathbf{q})$ is the surface response of the equivalent block (Fig. S1(D)) in the frequency domain. $M_{zz}(\mathbf{q})$ depends on the rheological and geometrical properties of the blocks (Fig. S1(C) but also Fig. S2(A)), and its formulation is summarized below for completeness.

Finally, the relation between separation $u(\mathbf{x})$ and contact pressure $\sigma_c(\mathbf{x})$ is calculated within the Derjaguin's approximation (5), and it can be written in term of a generic interaction law (6)

$$\sigma_c(u) = f(u). \qquad [A4]$$

In this work we have adopted the (integrated) repulsive term of the L-J potential in Eq. A4 to simulate the adhesionless interaction. The relation between separation $u(\mathbf{x})$ and the electro-adhesive traction $\sigma_{adh}(\mathbf{x})$ is instead calculated in term of Maxwell stress (7)

$$\sigma_{adh}(u) = -\frac{1}{2}\epsilon_0 V_0^2 \frac{1}{(u+h_0)^2} \qquad [A5]$$

where h_0 is defined in the main text.

Eqs. A1 to A5 are discretized on a regular square mesh of grid size δ in term of a residuals molecular dynamics process (RMD) (3, 6), and solved with a velocity Verlet integration scheme. The simulation is performed by a stepwise decrease of the average interface separation until a certain normalized contact area is reached. In order to take into account the surface plasticity, the plastic displacement field w_{pl} is locally incremented in order for the unilateral constraint $\sigma_c(\mathbf{x}) \le p_{pl}$ to hold, where p_{pl} is the surface hardness (limit contact pressure for surface plasticity).

We now report a summary of the main formulas needed to calculate $M_{zz}(\mathbf{q})$ for a layered solid. We first consider the generic case of a linearly viscoelastic infinitely wide slab of thickness d, see Fig. S2(B) and Ref. (3). By considering the

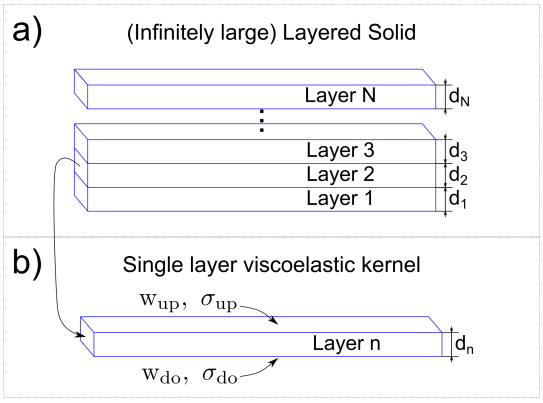

Fig. S2. Schematic of a infinitely-wide slab of finite thickness d, characterized by a linear viscoelastic rheology. σ_{up} (σ_{do}) and w_{up} (w_{do}) are, respectively, the stress and displacement fields on the top $z = 0$ (bottom $z = -d$) surface.

following Fourier transform ($t \to \omega$ and $\mathbf{x} \to \mathbf{q}$)

$$\mathbf{w}(\mathbf{q},z,\omega) = \frac{\int dt \int d^2x\; \mathbf{w}(\mathbf{x},z,t)\, e^{-i(\mathbf{q}\cdot\mathbf{x}-\omega t)}}{(2\pi)^3}$$

$$\mu(\omega) = \int dt\; \mu(t)\, e^{-i(-\omega t)}$$

and, inversely,

$$\mu(t) = (2\pi)^{-1} \int d\omega \; e^{i(-\omega t)} \mu(\omega)$$

$$\mathbf{w}(\mathbf{x}, z, t) = \int d\omega \int d^2q \; \mathbf{w}(\mathbf{q}, z, \omega) \, e^{i(\mathbf{q}\cdot\mathbf{x} - \omega t)},$$

the relation between the stress and displacement fields on the top ($z = 0$) and bottom surface ($z = -d$), in the limit of quasi-static interaction [i.e. $\omega/(qc) = v/c \ll 1$, see Ref. (4), where c is the generic sound speed] reads in matrix form

$$\begin{bmatrix} \boldsymbol{\sigma}_{\rm up}(\mathbf{q},\omega)/[E_{\rm r}(\omega)\, q/2] \\ \mathbf{w}_{\rm up}(\mathbf{q},\omega) \end{bmatrix} = \cosh(qd) \begin{bmatrix} \mathbf{M}_1 & \mathbf{M}_2 \\ \mathbf{M}_3 & \mathbf{M}_4 \end{bmatrix} \begin{bmatrix} \boldsymbol{\sigma}_{\rm do}(\mathbf{q},\omega)/[E_{\rm r}(\omega)\, q/2] \\ \mathbf{w}_{\rm do}(\mathbf{q},\omega) \end{bmatrix}, \tag{A6}$$

where $\mathbf{M}_j[\mathbf{q}d, \nu(\omega)]$ is a 3 by 3 matrix. $\boldsymbol{\sigma}_{\rm up}$ ($\boldsymbol{\sigma}_{\rm do}$) and $\mathbf{w}_{\rm up}$ ($\mathbf{w}_{\rm do}$) are, respectively, the stress and displacement fields on the top (bottom) surface, see Fig. S2(B). $E_{\rm r}(\omega) = E(\omega)/\left[1-\nu(\omega)^2\right]$ is the complex reduced elastic modulus, $\bar{q} = qd$ (similarly for $\bar{q}_x$ and $\bar{q}_y$), $\tilde{q} = \tanh\bar{q}$, $p(\omega) = 1-\nu(\omega)$, $p_0 = 1-\nu_0$ [with $\nu_0 = \nu(\omega \to 0)$] and where we have defined

$$m = p/p_0, \;\; n = [1-2\nu(\omega)]/[1-2\nu_0], \;\; \gamma = n/m, \tag{A7}$$

$$\beta = \frac{1-4\nu p_0}{[1-2\nu(\omega)][1-2\nu_0]}.$$

Note that m, n, γ and β depend on the frequency ω through the dependence on $\nu(\omega)$. The matrix $\mathbf{M}_i$, $i = 1..4$, reads

$$M_1 = I + (2\bar{q}p_0)^{-1} \begin{bmatrix} \bar{q}_x^2\tilde{q} & \bar{q}_x\bar{q}_y\tilde{q} & -i\bar{q}_x\gamma[\bar{q}-(1-2\nu_0)\tilde{q}] \\ \bar{q}_x\bar{q}_y\tilde{q} & \bar{q}_y^2\tilde{q} & -i\bar{q}_y\gamma[\bar{q}-(1-2\nu_0)\tilde{q}] \\ -i\bar{q}_x[\bar{q}+\beta(1-2\nu_0)\tilde{q}] & -i\bar{q}_y[\bar{q}+\beta(1-2\nu_0)\tilde{q}] & -\gamma\bar{q}^2\tilde{q} \end{bmatrix}, \tag{A8}$$

$$M_2 = \bar{q}^{-2} \begin{bmatrix} (n\bar{q}+\tilde{q})\bar{q}_x^2 + p\tilde{q}\bar{q}_y^2 & \bar{q}_x\bar{q}_y(n\bar{q}+\nu\tilde{q}) & -im\bar{q}_x\bar{q}^2\tilde{q} \\ \bar{q}_x\bar{q}_y(n\bar{q}+\nu\tilde{q}) & p\tilde{q}\bar{q}_x^2 + (n\bar{q}+\tilde{q})\bar{q}_y^2 & -im\bar{q}_y\bar{q}^2\tilde{q} \\ -in\bar{q}_x\bar{q}^2\tilde{q} & -in\bar{q}_y\bar{q}^2\tilde{q} & -m\bar{q}^2(\bar{q}-\tilde{q}/n) \end{bmatrix}, \tag{A9}$$

$$M_3 = (2\bar{q}mp_0)^{-2} \begin{bmatrix} 4p\tilde{q}\bar{q}^2 + m(\bar{q}-\tilde{q})\bar{q}_x^2 & m\bar{q}_x\bar{q}_y(\bar{q}-\tilde{q}) & -in\bar{q}_x\bar{q}^2\tilde{q} \\ m\bar{q}_x\bar{q}_y(\bar{q}-\tilde{q}) & 4p\tilde{q}\bar{q}^2 + m(\bar{q}-\tilde{q})\bar{q}_y^2 & -in\bar{q}_y\bar{q}^2\tilde{q} \\ -im\bar{q}_x\bar{q}^2\tilde{q} & -im\bar{q}_y\bar{q}^2\tilde{q} & -\gamma\bar{q}^2[m(\bar{q}+\tilde{q})-4p\tilde{q}] \end{bmatrix} \tag{A10}$$

$$M_4 = I + (2\bar{q}p_0)^{-1} \begin{bmatrix} \gamma\bar{q}_x^2\tilde{q} & \gamma\bar{q}_x\bar{q}_y\tilde{q} & -i\bar{q}_x[\bar{q}+(1-2\nu_0)\tilde{q}] \\ \gamma\bar{q}_x\bar{q}_y\tilde{q} & \gamma\bar{q}_y^2\tilde{q} & -i\bar{q}_y[\bar{q}+(1-2\nu_0)\tilde{q}] \\ -i\bar{q}_x\gamma[\bar{q}-\beta(1-2\nu_0)\tilde{q}] & -i\bar{q}_y\gamma[\bar{q}-\beta(1-2\nu_0)\tilde{q}] & -\bar{q}^2\tilde{q} \end{bmatrix}. \tag{A11}$$

Again here $M_j = M_j(\omega)$ through the frequency dependence of the Poisson's ratio.

In the case the frequency variation of the lateral contraction can be neglected, i.e. $\nu(\omega) = \nu = \nu_0$, we have that $m = n = \beta = \gamma = 1$ (and $p_0 = p$) and the Eqs. A8-A11 simplify to

$$M_1 = I + (2\bar{q}p)^{-1} \begin{bmatrix} \bar{q}_x^2\tilde{q} & \bar{q}_x\bar{q}_y\tilde{q} & -i\bar{q}_x[\bar{q}-(2p-1)\tilde{q}] \\ \bar{q}_x\bar{q}_y\tilde{q} & \bar{q}_y^2\tilde{q} & -i\bar{q}_y[\bar{q}-(2p-1)\tilde{q}] \\ -i\bar{q}_x[\bar{q}+(2p-1)\tilde{q}] & -i\bar{q}_y[\bar{q}+(2p-1)\tilde{q}] & -\bar{q}^2\tilde{q} \end{bmatrix}$$

$$M_2 = \bar{q}^{-2} \begin{bmatrix} (\bar{q}+\tilde{q})\bar{q}_x^2 + p\tilde{q}\bar{q}_y^2 & \bar{q}_x\bar{q}_y(\bar{q}+\nu\tilde{q}) & -i\bar{q}_x\bar{q}^2\tilde{q} \\ \bar{q}_x\bar{q}_y(\bar{q}+\nu\tilde{q}) & p\tilde{q}\bar{q}_x^2 + (\bar{q}+\tilde{q})\bar{q}_y^2 & -i\bar{q}_y\bar{q}^2\tilde{q} \\ -i\bar{q}_x\bar{q}^2\tilde{q} & -i\bar{q}_y\bar{q}^2\tilde{q} & -\bar{q}^2(\bar{q}-\tilde{q}) \end{bmatrix}$$

$$M_3 = (2\bar{q}p)^{-2} \begin{bmatrix} 4p\tilde{q}\bar{q}^2 + (\bar{q}-\tilde{q})\bar{q}_x^2 & \bar{q}_x\bar{q}_y(\bar{q}-\tilde{q}) & -i\bar{q}_x\bar{q}^2\tilde{q} \\ \bar{q}_x\bar{q}_y(\bar{q}-\tilde{q}) & 4p\tilde{q}\bar{q}^2 + (\bar{q}-\tilde{q})\bar{q}_y^2 & -i\bar{q}_y\bar{q}^2\tilde{q} \\ -i\bar{q}_x\bar{q}^2\tilde{q} & -i\bar{q}_y\bar{q}^2\tilde{q} & -\bar{q}^2[(\bar{q}+\tilde{q})-4p\tilde{q}] \end{bmatrix},$$

with $M_1 = M_4^T$.

Now, in Fig. S2(A) we show the schematic of the generic composite slab with a step-wise graded rheology, with $j = 1..n..N$ bonded layers. We first assume the generic layer $(n-1)$ to be described by the general stress-displacement relation

$$\mathbf{w}_{\rm up}(\mathbf{q},\omega) = [\mathbf{M}]^{(n-1)} \frac{\boldsymbol{\sigma}_{\rm up}(\mathbf{q},\omega)}{[E_{\rm r}(\omega)]^{(n-1)}\, q/2},$$

where $\mathbf{M}$ is a 3 by 3 matrix. Imposing the continuity of stress and displacement between layer $(n-1)$ and (n), and by using Eq. A6, we get for the layer (n)

$$\mathbf{w}_{\rm up}(\mathbf{q},\omega) = \left[\mathbf{M}_3 + \frac{E_{\rm r}(\omega)}{[E_{\rm r}(\omega)]^{n-1}}\mathbf{M}_4[\mathbf{M}]^{n-1}\right]\left[\mathbf{M}_1 + \frac{E_{\rm r}(\omega)}{[E_{\rm r}(\omega)]^{n-1}}\mathbf{M}_2[\mathbf{M}]^{n-1}\right]^{-1} \frac{\boldsymbol{\sigma}_{\rm up}(\mathbf{q},\omega)}{E_{\rm r}(\omega)\, q/2},$$

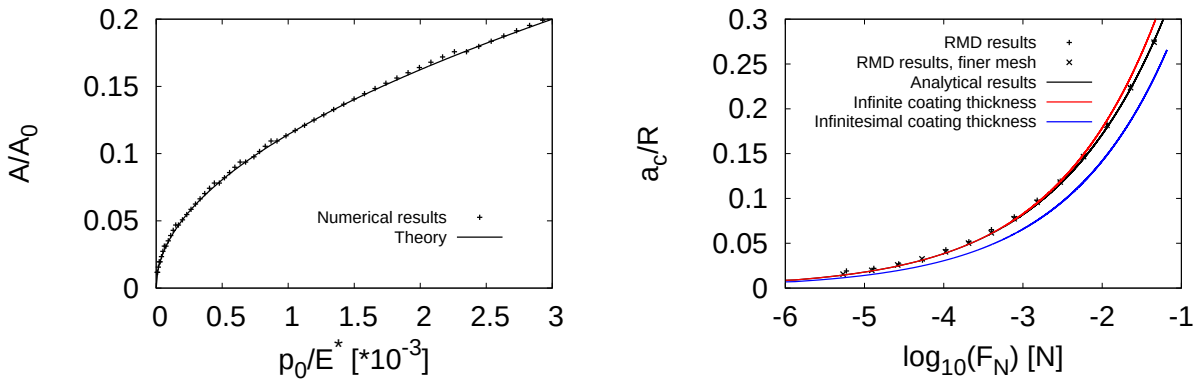

(a) Westergaard contact problem

(b) Rigid ball in normal contact against a coated elastic half space

Fig. S3. (a) Normalized contact area A/A_0 as a function of the normalized squeezing pressure p_0/E^* for the Westergaard sinus contact solution. Here the ratio between the sinus amplitude h and wavelength λ is $h/\lambda = 0.01$. The solid line is the analytical prediction, whereas dots are from the RMD model. (b) Normalized contact radius a_c/R as a function of the normal force F_N in logaritmic scale. For a point contact constituted by a rigid smooth ball squeezed against a coated elastic half space. The coating (bulk) elastic modulus and Poisson's ratio are $E_c = 1$ MPa ($E_b = 2$ MPa) and $\nu_c = 0.49$ ($\nu_b = 0.49$), respectively. The coating thickness is 200 μm and the ball radius 1 mm. The solid black line is the analytical model prediction, whereas dots are from the RMD model (at increasing mesh resolution). The red and blue curves are instead Hertzian results, obtained for an infinite and infinitesimal coating thickness, respectively.

where $\mathbf{M}_{i=1..4}$ and $E_r(\omega)$ are for the layer (n) (the superscript (n) has been omitted for simplicity). Thus $\mathbf{M}$ for the layer (n) reads

$$[\mathbf{M}]^{(n)} = \left[\mathbf{M}_3 + \frac{E_r(\omega)}{[E_r(\omega)]^{(n-1)}}\mathbf{M}_4[\mathbf{M}]^{(n-1)}\right]\left[\mathbf{M}_1 + \frac{E_r(\omega)}{[E_r(\omega)]^{(n-1)}}\mathbf{M}_2[\mathbf{M}]^{(n-1)}\right]^{-1}, \quad [A12]$$

resulting in

$$\mathbf{w}_{up} = [\mathbf{M}]^{(n)} \frac{\boldsymbol{\sigma}_{up}}{[E_r(\omega)]^{(n)} q/2}. \quad [A13]$$

Eq. A12 shows that the surface response of a stepwise-graded composite can be determined with a simple recursive calculation.

Finally, for the stepwise graded composite with N-layers

$$M_{zz}(\mathbf{q},\omega) = \frac{2}{q}\frac{[\mathbf{M}(\mathbf{q},\omega)]^{(N)}_{3,3}}{[E_r(\omega)]^{(N)}}, \quad [A14]$$

where $[\mathbf{M}]^{(1)}$ [innermost layer, needed to initialize Eq. A12] is obtained depending on the adopted BCs (note: $M_{zz}(\mathbf{q})$ of Eq. A3 is given by $M_{zz}(\mathbf{q},\omega)$ of Eq. A14 for $\omega = 0$). For $\mathbf{w}_{do}(\mathbf{q},\omega) = 0$ we have

$$[\mathbf{M}]^{(1)} = \mathbf{M}_3\mathbf{M}_1^{-1},$$

whereas for $\sigma_{do}(\mathbf{q},\omega) = 0$ we have

$$[\mathbf{M}]^{(1)} = \mathbf{M}_4\mathbf{M}_2^{-1},$$

for $q \neq 0$. We observe that in the simplest case where the bulk is an elastic half-space

$$M_{zz}(\mathbf{q}) = 2/[|\mathbf{q}| E_r],$$

where $E_r = E/\left(1-\nu^2\right)$ is the reduced Young's modulus, ν is the Poisson's ratio.

It is also interesting to calculate the stress and displacement fields acting at intermediate layers across the graded solid. Indeed, the stress (or deformation) variations across the solid is of large interest since it could be linked to the stress acting on the nerve cells at different depths from the contact surface. For the generic layer of index n, by using Eqs. A6 and A13, after some manipulations, one can calculate (recursively) the stress acting on the bottom surface $\sigma_{do}(\mathbf{q},\omega)$ from the following equation

$$N\sigma_{up}(\mathbf{q},\omega) = \cosh(qd) M_1\sigma_{do}(\mathbf{q},\omega), \quad [A15]$$

where

$$N = I + \left(M_3M_1^{-1} - M_4M_2^{-1}\right)^{-1}\left(M - M_3M_1^{-1}\right), \quad [A16]$$

and where the index n has been dropped in the notation of Eqs. A15 and A16.

Model validation. In this section, we compare the RMD results with the predictions of existing analytical contact mechanics results, in order to validate the contact algorithm (ability to detect contact borders) as well as the layered-bulk surface kernel (to test the recursive Eq. A14).

The fist validation is thus made against a very simple periodic contact geometry, the Westergaard (sinus) roughness in contact with a linear elastic half plane. Thus, in Fig. S3(a) we report the normalized contact area A/A_0 as a function of the normalized squeezing pressure p_0/E^* for the Westergaard geometry, for a ratio between the sinus roughness amplitude h and wavelength λ given by $h/\lambda = 0.01$. In the figure, the solid line is the analytical prediction (1), whereas dots are from the RMD model run with 256 divisions over the wavelength. The simulation is run up to a small normalized contact area ($A/A_0 < 0.2$), thus for contacts involving a reduced number of contacting points, in order to check the contact area accuracy for small contact patches. The agreement is satisfactory.

Now, to verify the RMD model predictions for the case of graded rheology, we make use of the analytical model provided for the case of an elastically-coated elastic half space in point contact with a rigid smooth ball (thus, similar to the Hertzian circular contact geometry but with a coated half space), see Refs. (1). Thus, in Fig. S3(b) we show the normalized contact radius a_c/R as a function of the normal force F_N in logaritmic scale, for a point contact constituted by a rigid smooth ball squeezed against a coated elastic half space. The coating (bulk) elastic modulus and Poisson's ratio are $E_c = 1$ MPa ($E_b = 2$ MPa) and $\nu_c = 0.49$ ($\nu_b = 0.49$), respectively. The coating thickness is 200 μm and the ball radius 1 mm. The solid black line is the analytical model prediction (1), whereas dots are from the RMD model (at increasing mesh resolution). The red and blue curves are instead Hertzian results, obtained for an infinite and infinitesimal coating thickness, respectively. Also here the agreement is satisfactory, confirming the overall accuracy of the computational contact model.

On the voltage frequency dependency of friction

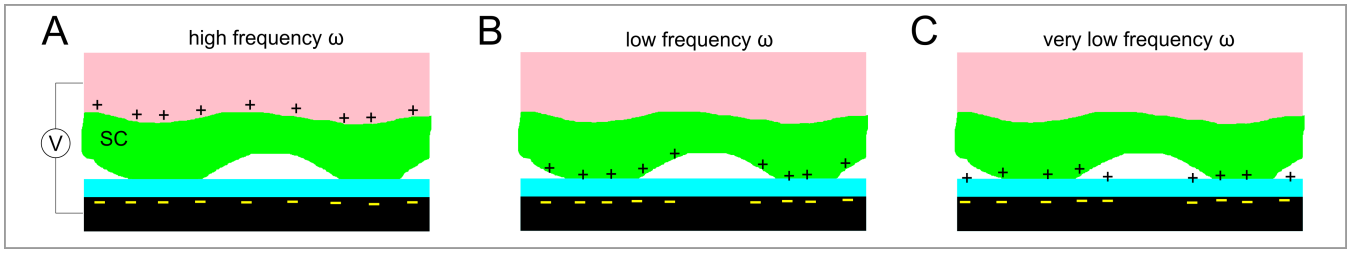

Fig. S4. Distribution of charges at the contact between the skin (green and pink) and a touchscreen (black and blue) when an oscillating electric potential $\phi = V_0\cos(\omega t)$ acts between the skin and the touchscreen. The SC of the skin has a finite electric conductivity. (*A*) When the frequency ω is very high there is not enough time for charges to drift through the SC during the time period of an oscillation $T = 2\pi/\omega$. (*B*) As ω decreases, charges can drift to the bottom surface of the skin. If the electric resistance of the glass surface layer is infinite, no charges can flow to the glass surface of the touchscreen. (C) However, the glass surface layer has a finite surface conductivity, and if the frequency ω is small enough, the charges will drift to the glass surface, which will reduce the electroadhesive force between the finger and the touchscreen to nearly zero.

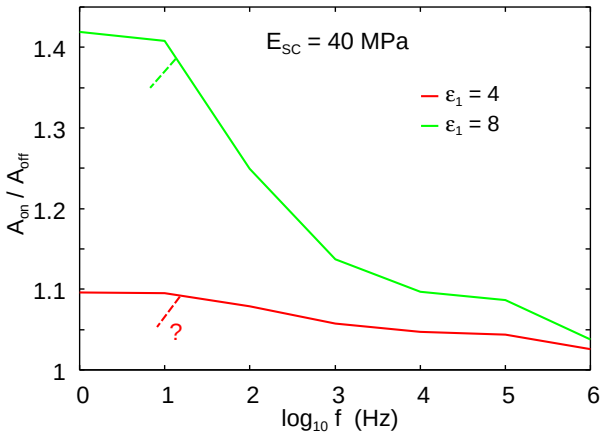

Fig. S5. The calculated dependency of the contact area on the frequency $f = \omega/(2\pi)$ of the oscillating electric potential $\phi = V_0\cos(\omega t)$. The A_{on}/A_{off} is the ratio between the real contact area with electroadhesion to that without electroadhesion. See text for details.

Fig. S4 shows the spatial distribution of charges close to the contact interface when the frequency of the oscillating applied voltage is reduced. (A) For high frequencies there is no time for the charges on the skin side to drift to the outer skin surface. When the frequency is reduced, charges drift to the outer surface of the SC (B) and at very low frequency the charges may drift onto the touch screen glass surface (C), which would result in a drop in the electroadhesion force.

Fig. S5 shows the frequency dependency of the calculated ratio between the (time averaged) contact area when the applied voltage is turned on and when it is turned off. We have assumed that the electric insulating layer on the touch screen has the dielectric function $\epsilon_1 = 4$ and 8. We have assumed that there is no transfer of charges from the skin to the touch screen glass surface, so the electroadhesion force is largest at low frequencies where the charges on the skin are located on the outer surface of the SC.

The probability density function of interface electro-adhesive stress and electric field

The multiscale roughness of real surfaces results in contact mechanics properties which vary over a wide range of parameters values. To illustrate this, let $P_u(u)$, $P_E(E)$ and $P_\sigma(\sigma)$ be the probability distributions for the separation u, the electric field strength in the air-gap E, and the attractive electric stress σ acting on the outer surface of the skin from the touchscreen. The probability distributions are assumed to be normalized so that, e.g.,

$$\int_0^\infty du\ P_u(u) = \int_0^\infty dE\ P_E(E) = 1. \tag{B1}$$

Since

$$E = \frac{V_0}{u + h_0} \tag{B2}$$

we get

$$dE = -\frac{V_0}{(u+h_0)^2} du.$$

Using this gives

$$\int_0^\infty dE\ P_E = \int_0^\infty du\ P_E \frac{V_0}{(u+h_0)^2}.$$

Comparing this to Eq. B1 gives

$$P_E = \frac{(u+h_0)^2}{V_0} P_u. \tag{B3}$$

Using Eq. B2 and B3 it is easy to plot P_E as a function of E given P_u as a function of u.

Next let us derive the distribution of attractive stress due to the electric field in the air gap. The electric stress

$$\sigma = \frac{1}{4}\frac{\epsilon_0 V_0^2}{(u+h_0)^2}. \tag{B4}$$

Thus we get

$$d\sigma = -\frac{1}{2}\frac{\epsilon_0 V_0^2}{(u+h_0)^3} du.$$

From

$$\int_0^\infty du\ P_u(u) = \int_0^\infty d\sigma\ P_\sigma(\sigma) = \int_0^\infty du\ P_\sigma \frac{1}{2}\frac{\epsilon_0 V_0^2}{(u+h_0)^3}$$

we get

$$P_\sigma = \frac{2(u+h_0)^3}{\epsilon_0 V_0^2} P_u. \tag{B5}$$

Using Eq. B4 and B5 it is easy to plot P_σ as a function of σ given P_u as a function of u.

In Fig. S6 we show the probability distributions of interfacial separation when the finger is squeezed with the nominal pressure $p_0 = 15.5$ kPa against the touchscreen. We have assumed $E_{\rm SC} = 40$ MPa and $h_0 = 0.2$ μm as in Fig. 3(C) in the main text. We show results when the applied voltage is $V_0 = 0$ and $V_0 = 100$ V. When the electric voltage is applied, the effective squeezing force (and the area of real contact) roughly increases with a factor of 2, but the interfacial surface separation decreases rather small.

Fig. S7 shows the probability distribution of electric field strength. The highest electric field occurs in the vacuum gap where the interfacial separation is small, but this region (which consists of the area of contact and the rim-area) occupies only a small part of the nominal contact area.

Fig. S8 shows the distribution of (repulsive) stress acting in the area of real contact. Note that the stress is very high, of order the Young's modulus of the skin SC. This result follows immediately from contact mechanics theory. Thus, when the relative contact area is small as in the present case, the linear elastic contact mechanics predicts the relative contact area $A/A_0 \approx 2p_0/(Eh')$ where h' is the rms surface slope (which is of order unity in our case). The normal (applied) force $F_0 = A_0 p_0$ so the average stress in the asperity contact regions $F_0/A \approx Eh'/2$ is of order the Young's modulus of the SC, as indeed observed in Fig. S8.

Fig. S9 shows the probability distribution of the adhesive electric stress acting on the outer skin surface in the nominal skin-glass contact area. In most of the skin area the adhesive stress is very small, of order $1 - 100$ Pa, but this surface area gives a negligible contribution to the total attractive electrostatic force. This can be explained as follows.

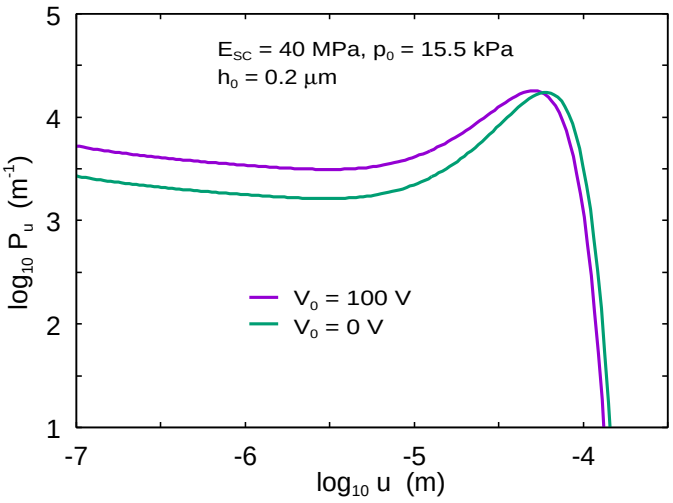

Fig. S6. The probability distribution $P_u(u)$ of interfacial separation for $E_{\rm SC} = 40$ MPa, $h_0 = 0.2$ μm, and the applied voltage amplitude $V_0 = 0$ and $V_0 = 100$ V. The logarithm of $P_u(u)$ is shown as a function of the logarithm of the interfacial separation.

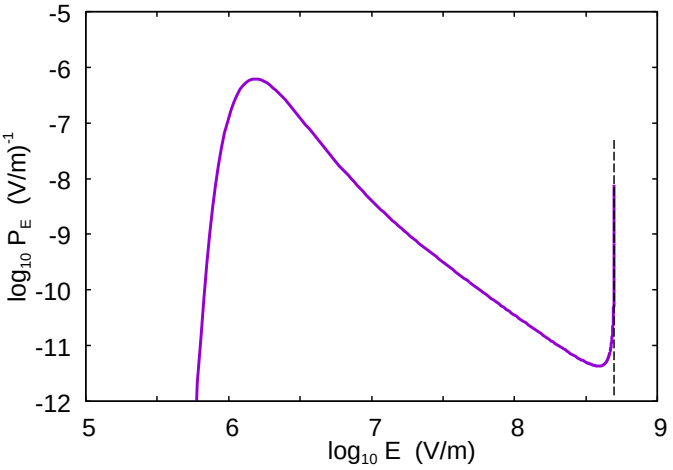

Fig. S7. The probability distribution $P_E(E)$ of electric field strength in the air gap for $E_{\rm SC} = 40$ MPa, $h_0 = 0.2$ μm, and the applied voltage amplitude $V_0 = 100$ V. The logarithm of $P_E(E)$ is shown as a function of the logarithm of the electric field strength. The vertical dashed line indicates the maximum electric field, $E = V_0/h_0$.

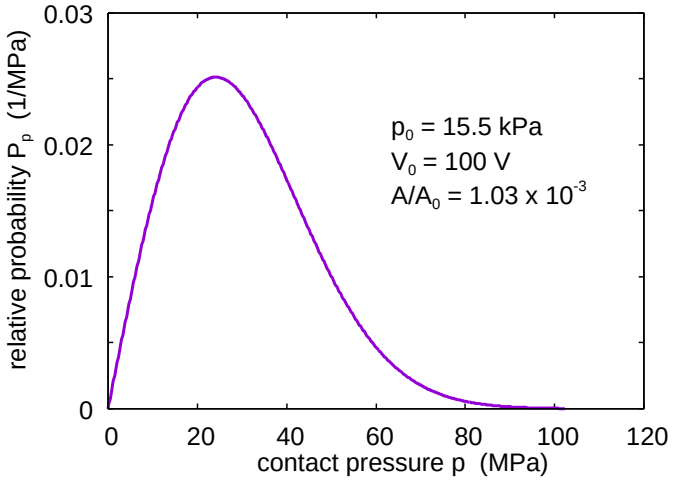

Fig. S8. The probability distribution $P_p(p)$ of contact pressures for $E_{\rm SC} = 40$ MPa, $h_0 = 0.2$ μm, and the applied voltage amplitude $V_0 = 100$ V.

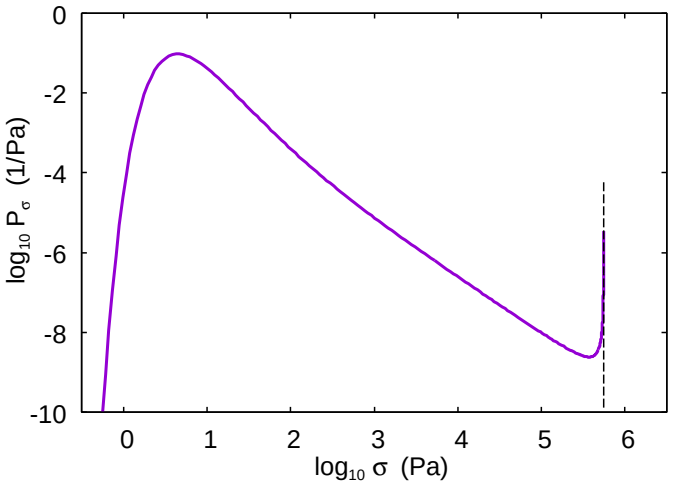

Fig. S9. The probability distribution $P_\sigma(\sigma)$ of the electric attraction stress for $E_{\rm SC} = 40$ MPa, $h_0 = 0.2$ μm, and the applied voltage amplitude $V_0 = 100$ V. The logarithm of $P_\sigma(\sigma)$ is shown as a function of the logarithm of the electric stress. The vertical dashed line indicates the maximum electric stress $\sigma = \epsilon_0 V_0^2/(4h_0^2)$.

To understand which region in space gives the largest contribution to the electric adhesion force, we consider the average adhesive stress

$$\langle\sigma\rangle = \int_0^\infty d\sigma\ \sigma P_\sigma(\sigma).$$

Let us introduce a new integration variable $x = \log_{10}(\sigma)$ so that $d\sigma = \ln(10)\sigma dx$ and

$$\langle\sigma\rangle = \int_{-\infty}^\infty dx\ S(x),$$

where

$$S = \ln(10)\sigma^2 P_\sigma(\sigma).$$

Thus $S(x)dx$ is the contribution to the average stress from the region where the logarithm of the stress is between $x = \log_{10}\sigma$ and $x + dx = \log_{10}\sigma + d\log_{10}\sigma$. In Fig. S10 we show $\log_{10}S$ as a function of $x = \log_{10}\sigma$. Clearly the most important contribution to the adhesive normal load comes from the region where the stress is close to the maximum stress $\sigma_{\rm max} = \epsilon_0 V_0^2/(4h_0^2)$, indicated by the vertical dashed line. This region in σ-space corresponds to the area of real contact and the region close to the area of real contact, where the skin-touchscreen surface separation is very small; this region is denoted as the rim-area.

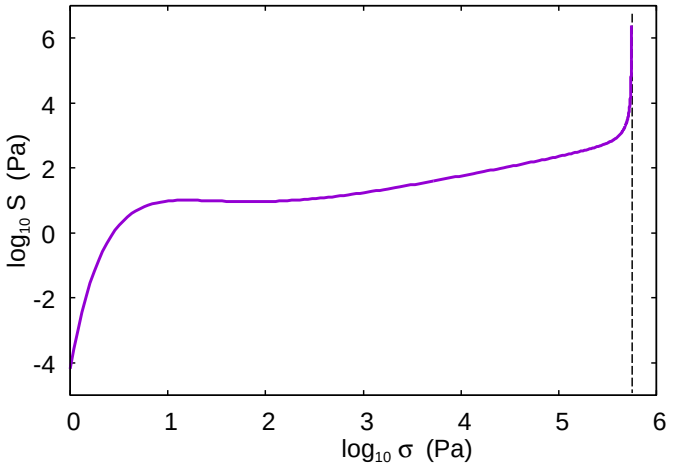

Fig. S10. The logarithm of the function S as a function of the logarithm of the electric stress (see text for details) for $E_{\rm SC} = 40$ MPa, $h_0 = 0.2$ μm, and the applied voltage amplitude $V_0 = 100$ V. The vertical dashed line indicates the maximum electric stress $\sigma = \epsilon_0 V_0^2/(4h_0^2)$.

The spatial distribution of the interfacial separation, and the spatial distribution of the attractive and repulsive surface stresses, depends on the realization of the randomly rough surface and is hence not predicted by the Persson's contact mechanics theory which only predicts ensemble averaged quantities. However, these quantities are easily predicted by (deterministic)

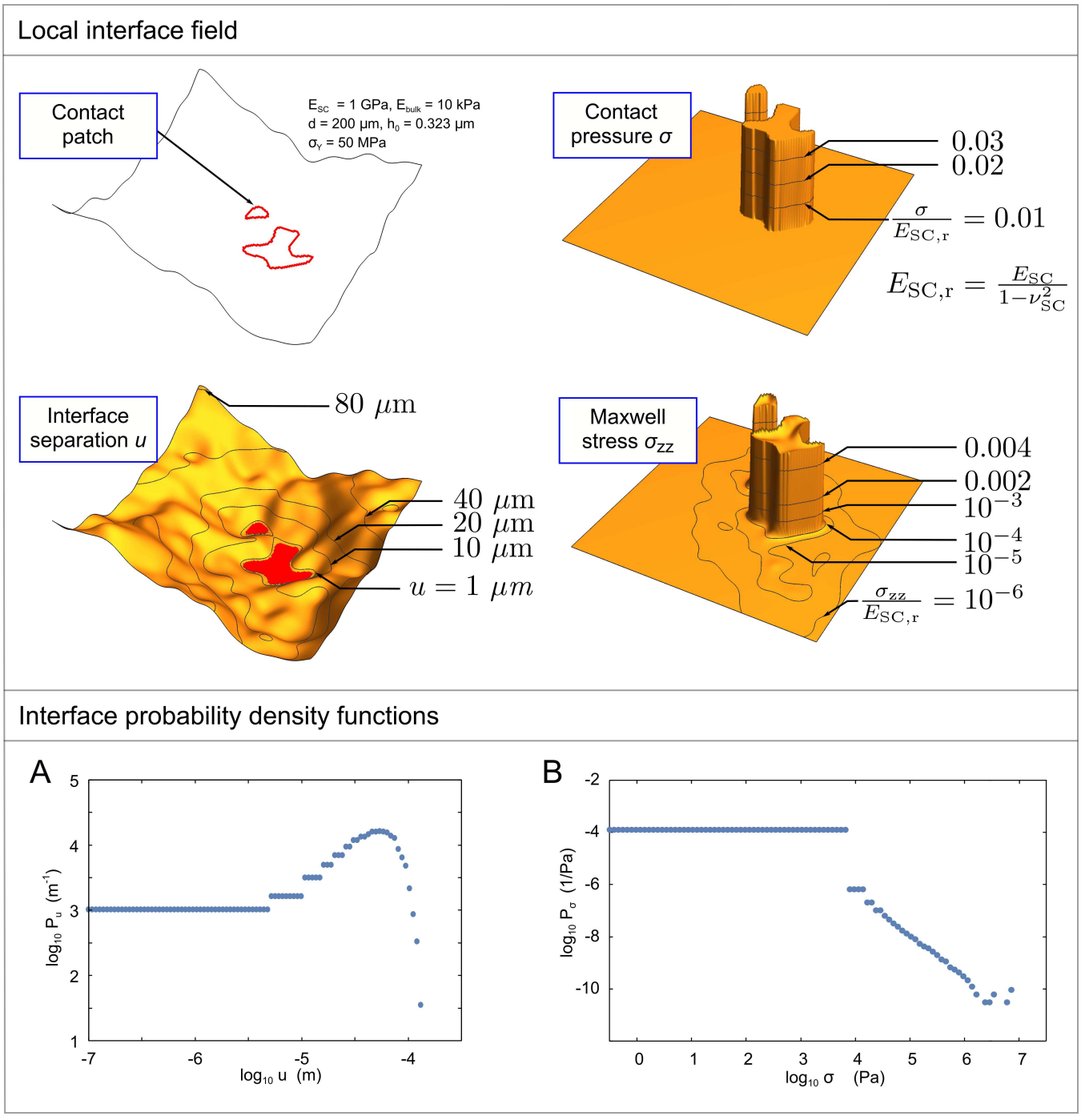

Fig. S11. Top panel: Contact pressure, interface separation and electro-adhesive stress acting on the magnified contact domain of Fig. 2C, as obtained with BEM simulations. Bottom panel: Probability density function of the interface separation (A) and electro-adhesive stress (B) as calculated with the BEM model for the system of Fig. 2D at $V_0 = 400$ V, for the largest normalized contact area. In (A) and (B), the strait (dotted) line at decreasing separation (A) or electro-adhesive stress (B) is due to the finite mesh size and separation field encountered in the numerical system.

computational contact methods, when applied to one realization of the rough surface. To illustrate this, we show some results from the BEM calculation for the surface considered in Fig. 2*B, C* and *D*.

For the contact parameters of Fig. 2 with $V_0 = 400$ V, in Fig. S11 we show in the top panel the contact pressure, interface separation and electro-adhesive stress acting on the magnified contact domain of Fig. 2*C* (obtained with BEM simulations). Moreover, for the same system, in the bottom panel of Fig. S11 we report the BEM-calculated probability density function (PDF) of the interface separation (*A*) and electro-adhesive stress (*B*). We observe that the interface separation (electro-adhesive stress) PDF reported in Fig. S11(*A*) (S11(*B*)) is in good qualitative agreement with the PDF calculated with the mean field theory in Fig. S6 (Fig. S9), when considering the different input contact parameters. We note, nevertheless, that the predicted PDFs show a poorer agreement at decreasing values of separation or electro-adhesive stress. This is easy to be understood. Indeed, at small separations, the numerical system probes the finite size effects (finite spatial resolution), resulting in a small statistical set available for the PDF generation. Similarly, at small electro-adhesive stresses, the numerical system probes a finite roughness height effect, i.e. the numerical separation field is always limited to a maximum value (the maximum roughness height) which depends on the specific roughness realization.

References

1. Johnson KL (1985) *Contact Mechanics*. (Cambridge University Press).
2. Persson BNJ (2000) *Sliding Friction: Physical Principles and Applications*. (Springer, Heidelberg).
3. Scaraggi M, Comingio D (2017) Rough contact mechanics for viscoelastic graded materials: The role of small-scale wavelengths on rubber friction. *International Journal of Solids and Structures* 125:276 – 296.
4. B.N.J. P (2001) Theory of rubber friction and contact mechanics. *Journal of Chemical Physics* 115(8):3840–3861.
5. Derjaguin B (1934) Untersuchungen über die reibung und adhäsion, iv. *Kolloid-Zeitschrift* 69(2):155–164.
6. Persson BNJ, Scaraggi M (2014) Theory of adhesion: Role of surface roughness. *The Journal of Chemical Physics* 141(12):124701.
7. Persson BNJ (2018) The dependency of adhesion and friction on electrostatic attraction. *J Chem Phys* 148(14):144701.